Angewandte Chemie International Edition
www.angewandte.org
How to cite: *Angew. Chem. Int. Ed.* **2025**, *64*, e202505580
doi.org/10.1002/anie.202505580

Nitrate Reduction

Efficient Ammonia Electrosynthesis from Pure Nitrate Reduction via Tuning Bimetallic Sites in Redox-Active Covalent Organic Frameworks

Zedong Zhang[+], Miao Wang[+], Hao-Ran Xing[+], Xiaocheng Zhou, Lei Gao, Shizheng Chen, Yinjuan Chen, Hui Xu, Wei Li, Shuai Yuan, Cheng-Hui Li, Zhong Jin,* and Jing-Lin Zuo**

Abstract: Electrocatalytic nitrate reduction reaction (NITRR) represents a promising approach for ammonia synthesis, but existing application has been constrained by the complex proton-coupled electron transfer and the sluggish kinetics induced by various intermediates. Herein, we synthesized a series of metalized covalent organic frameworks: NiTP-MTAPP MCOFs (M = 2H, Co, Cu, and Fe), based on dual redox-active centers: thiophene-substituted Ni-bis(dithiolene) ligand-Ni[$C_2S_2(C_4H_2SCHO)_2$]$_2$ and metallic porphyrin. Through regulating the adsorption and desorption of species at the catalytic sites, we have identified the optimal NITRR electrocatalyst: NiTP-CoTAPP MCOF, which achieved the highest faradaic efficiency (FE) of approximately 85.6% at −0.8 V (vs. RHE) in pure nitrate solution, with an impressive yield rate of 160.2 mmol h^{-1} $g^{-1}{}_{cat.}$ The generation of active hydrogen at [NiS_4] sites achieved dynamic equilibrium with the timely hydrogenation reaction at CoN_4 sites, effectively suppressing the hydrogen evolution reaction. Moreover, the incorporation of thiophene (TP) groups and metal ions facilitates charge transfer. Density functional theory (DFT) calculations demonstrated the reduction in energy barriers at different catalytic sites. The CoN_4-NiS_4 system exhibited the optimal adsorption-to-desorption capability and the lowest energy barrier (0.58 eV) for the rate-determining step (*NO → *HNO), which is supported by the moderate d-band center and Bader charge value.

Introduction

Ammonia (NH_3) has been extensively used in agricultural and industrial productions, driven by its high energy density and hydrogen content.[1–3] Currently, the highly energy-intensive Haber-Bosch process remains the predominant method for NH_3 production, but it also causes large-scale carbon dioxide emissions.[4–6] To effectively reduce the carbon footprint and sustainable production, electrocatalytic technology has garnered widespread attention. Unfortunately, due to the ultra-stable $-N{\equiv}N$ triple bond (941 kJ mol^{-1}), electrocatalytic nitrogen reduction reaction (NRR) is extremely challenging.[7–10] By contrast, nitrate reduction reaction (NITRR) offers a promising and alternative method for ammonia synthesis, which has the low dissociation energy (204 kJ mol^{-1}) of $-N{=}O$ bond and better aqueous solubility.[11–15] Moreover, nitrate is abundant in industrial wastewater and seriously harming the environment. NITRR can effectively deal with the pollution, and high value-added products also provide high atomic economy, which achieves a win–win situation.[4,16–18] Nonetheless, consistently synthesizing ammonia with good yields and faradaic efficiency (FE) values from pure nitrate feedstocks and consequently producing concentrated ammonia solutions to avoid additional separation expenses continues to pose a significant challenge.

Covalent organic frameworks (COFs) offer fascinating advantages, such as high specific surface areas, tunable pore structures, and enhanced electron/proton transport properties, making them promising candidates for molecular catalytic materials. In comparison to electrocatalysts such as alloys, metal nanoparticles, and metal oxides, COFs possess well-defined structures and offer relatively mild synthetic pathways.[19–23] Metalized covalent organic frameworks

---

[*] Z. Zhang[+], M. Wang[+], H.-R. Xing[+], X. Zhou, L. Gao, S. Chen, W. Li, S. Yuan, C.-H. Li, Z. Jin, J.-L. Zuo
State Key Laboratory of Coordination Chemistry, MOE Key Laboratory of Mesoscopic Chemistry, MOE Key Laboratory of High Performance Polymer Materials and Technology, Jiangsu Key Laboratory of Advanced Organic Materials, Institute of Theoretical and Computational Chemistry, School of Chemistry and Chemical Engineering, Nanjing University, Nanjing, Jiangsu 210023, P.R. China
E-mail: chli@nju.edu.cn
zhongjin@nju.edu.cn
zuojl@nju.edu.cn

Z. Jin
Suzhou Key Laboratory of Green Intelligent Manufacturing of New Energy Materials and Devices, Tianchang New Materials and Energy Technology Research Center, Institute of Green Chemistry and Engineering, School of Chemistry and Chemical Engineering, Nanjing University, Suzhou, Jiangsu 215163, P.R. China

Y. Chen, H. Xu
Key Laboratory of Advanced Catalytic Materials and Technology, Advanced Catalysis and Green Manufacturing Collaborative Innovation Center, School of Environmental & Safety Engineering, Changzhou University, Changzhou, Jiangsu 213164, P.R. China

[+] These authors contributed equally to this work.

Additional supporting information can be found online in the Supporting Information section

(MCOFs) exhibit excellent solvent stability (especially water stability) and provide additional metal active sites.[24–27] Additionally, metalloporphyrins have been used as redox-active units, driven by their unique electronic structures, which can effectively bind to the reactive substrate and promote electron transfer.[28,29] Fe, Co, Cu, and Ni ions are commonly employed to enhance the electronic properties, which find extensive application in catalytic processes such as the hydrogen evolution reaction (HER), oxygen evolution reaction (OER), oxygen reduction reaction (ORR), and carbon dioxide reduction reaction (CO_2RR).[30–36] NITRR involves multiple reaction paths with 9 protons and 8 electrons ($NO_3^- + 6H_2O + 8e^- \rightarrow NH_3 + 9OH^-$), and electrocatalysts with well-defined structures can help to understand the complex reaction mechanism.[37–40] Moreover, [Metal-N_4] units can interact with NO_3^- and facilitate its adsorption. This adsorption not only increases the concentration of the NO_3^- root around the catalyst but also weakens the —N—O bonding energy. The nitrosyl (NO) or hydroxylamine (NH_2OH) intermediates produced during the nitrate reduction can be stabilized by metalloporphyrin, making it further converted to NH_3 and improving the selectivity without generating N_2.[41–44]

Atomic-level dispersed catalysts have the maximum atomic utilization rate. Dual-atom catalysts (DAC) have active sites composed of two metal catalytic atoms, which can reduce the reaction energy barrier.[45–47] Similarly, bimetallic MCOFs can provide uniform and well-dispersed active centers, while the catalytic sites exhibit reduced tendencies for aggregation.[48–51] Furthermore, it is documented that the Ni catalytic sites can adsorb the intermediates and provide enough active hydrogen (·H) to promote the hydrogenation of $^*NO_x$.[52,53] In this work, Ni has been introduced into the thiophene-substituted dithiolene ligand-Ni[$C_2S_2(C_4H_2SCHO)_2$]$_2$, followed by coupling with the presynthesized electron-deficient metalloporphyrin (CoTAPP, [5,10, 15,20-Tetrakis-(4-aminophenyl)-porphyrin-cobalt]; CuTAPP and FeTAPP), to obtain a series of MCOFs (NiTP-CoTAPP, NiTP-CuTAPP, and NiTP-FeTAPP), which achieved a uniform dispersion of the bimetal catalytic sites at the atomic level. The recent studies revealed that the electron deficiency of catalysts enhances the repelling effect with counter K^+ ions. This effect is driven by the electric-field-dependent synergy between interfacial water and cations, significantly facilitating the process of nitrate reduction. Further, assessments of NITRR revealed their excellent performances; notably, the NiTP-CoTAPP achieved the highest faradaic efficiency (FE) of approximately 85.6% at −0.8 V (vs. RHE) for NH_3 production in pure nitrate solution of 0.5 M KNO_3, with an impressive yield rate of 160.2 mmol h^{-1} $^{-1}{}_{\text{cat.}}$ The N—O bond strength was weakened due to the high density of S/N-heteroatoms content. [NiS_4] sites mimicked nitrite reductase, further promoting the conversion of NO_2^- intermediates and achieving dynamic equilibrium with the timely hydrogenation reaction through the whole CoN_4–NiS_4 system, which effectively suppressed the HER. Our results indicated that the modular design of bimetallic MCOFs, by incorporating metal-containing ligands with presynthesized metalloporphyrin, can screen out electrocatalysts with optimal NITRR catalytic performance. DFT calculations reveal that NiTP-MTAPP (M = Co, Cu, and Fe) exhibits distinct reaction pathways and rate-determining steps in catalysis further rationalizing the experimental findings.

Results and Discussion

Design and Synthesis of NiTP-MTAPP MCOFs (M = 2H, Co, Cu, and Fe)

Ni-bis(dithiolene) units possess a π-conjugated electronic structure and abundant redox activity. Recently, the MCOFs (NiPh-CoTAPP MCOF) constructed from the ligand-Ni[$C_2S_2(C_6H_4CHO)_2$]$_2$ and cobalt–porphyrin units have been confirmed to be ideal ORR/OER bifunctional cathode catalysts in Li-O_2 batteries.[31] And the bimetallic Zn_5-NiS_4TP MOF cascade catalytic NITRR based on the redox ligand-Ni[$C_2S_2(C_4H_2SCOOH)_2$]$_2$ has also been reported.[54] Incorporating thiophene groups into Ni-bis(dithiolene) units to synthesize Ni[$C_2S_2(C_4H_2SCHO)_2$]$_2$ (Figure S1a) and then constructing a series of 2D MCOFs, which can accurately modulate the electronic environment, facilitate charge transfer and increase the carrier concentration.[55–57] The redox activity of [NiS_4TP] units (Figure S1b) was studied by the solid-state cyclic voltammetry (CV), and two quasi-reversible redox peaks appeared at −0.81 and −0.15 V (vs. Fc/Fc^+; in 0.1 M $LiBF_4$/DMF; the scan rate: 200 mV s^{-1}). Additionally, the five-membered heterocyclic structure may provide more diverse pore architectures in the construction of MCOFs. As expected, the solvothermal reaction of Ni[$C_2S_2(C_4H_2SCHO)_2$]$_2$ with presynthesized M-TAPP at 120 °C for 5 days gave rise to four isostructural MCOFs, namely, NiTP-TAPP, NiTP-CoTAPP, NiTP-CuTAPP, and NiTP-FeTAPP (Figure 1).

Structure and Characterization

The structures of NiTP-TAPP, NiTP-CoTAPP, NiTP-CuTAPP, and NiTP-FeTAPP were highly defined, which was confirmed by powder X-ray diffraction (PXRD) analysis, and structural simulations were performed by Material Studio. The isostructural MCOFs all adopt a 2D ***sql*** topology with the AA-stacking mode. Thiophene-substituted Ni-bis(dithiolene) units and metalloporphyrin blocks were alternately arranged. For NiTP-TAPP, Pawley refinement based on the $P1$ space group provided lattice parameters of $a = 28.19$ Å, $b = 21.64$ Å, $c = 6.34$ Å, $\alpha = 58°$, $\beta = 55°$, and $\gamma = 90°$ (Figure S2, $R_p = 1.05\%$ and $R_{wp} = 1.37\%$). The diffraction peaks at 5.23°, 8.14°, and 9.64° were assigned to the (1-10), (110), and (120) facets, respectively. All NiTP-MTAPP MCOFs (M = Co, Cu, and Fe) exhibited similar diffraction peaks, which could be assigned to similar facets. Take NiTP-CoTAPP, for example, Pawley refinement based on the P1 space group provided lattice parameters of $a = 28.22$ Å, $b = 21.54$ Å, $c = 6.33$ Å, $\alpha = 59°$, $\beta = 55°$, and $\gamma = 90°$ (Figure 2a, $R_p = 1.07\%$ and $R_{wp} = 1.46\%$ for NiTP-CoTAPP; Figure 2b, $R_p = 1.28\%$ and

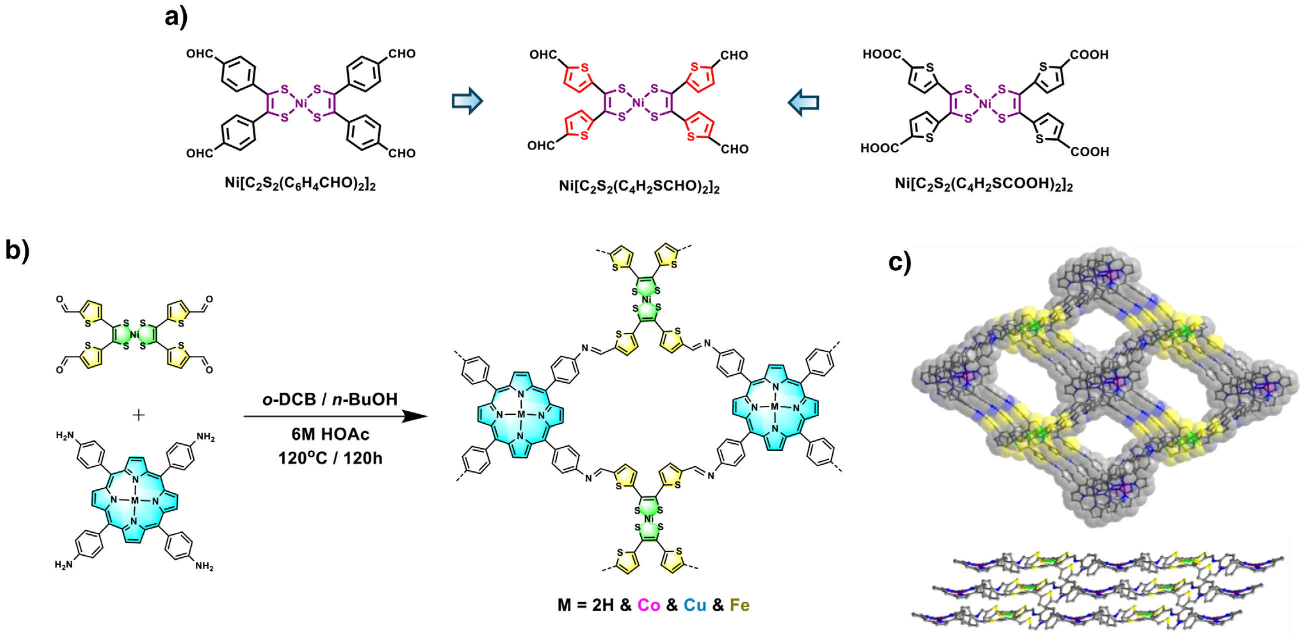

Figure 1. a) The design and structure of $Ni[C_2S_2(C_4H_2SCHO)_2]_2$. b) Schematic diagram of the synthesis of NiTP-MTAPP MCOFs (M = 2H, Co, Cu, and Fe). c) Extended structures of NiTP-CoTAPP (*c*-axis) and view along the *a*-axis.

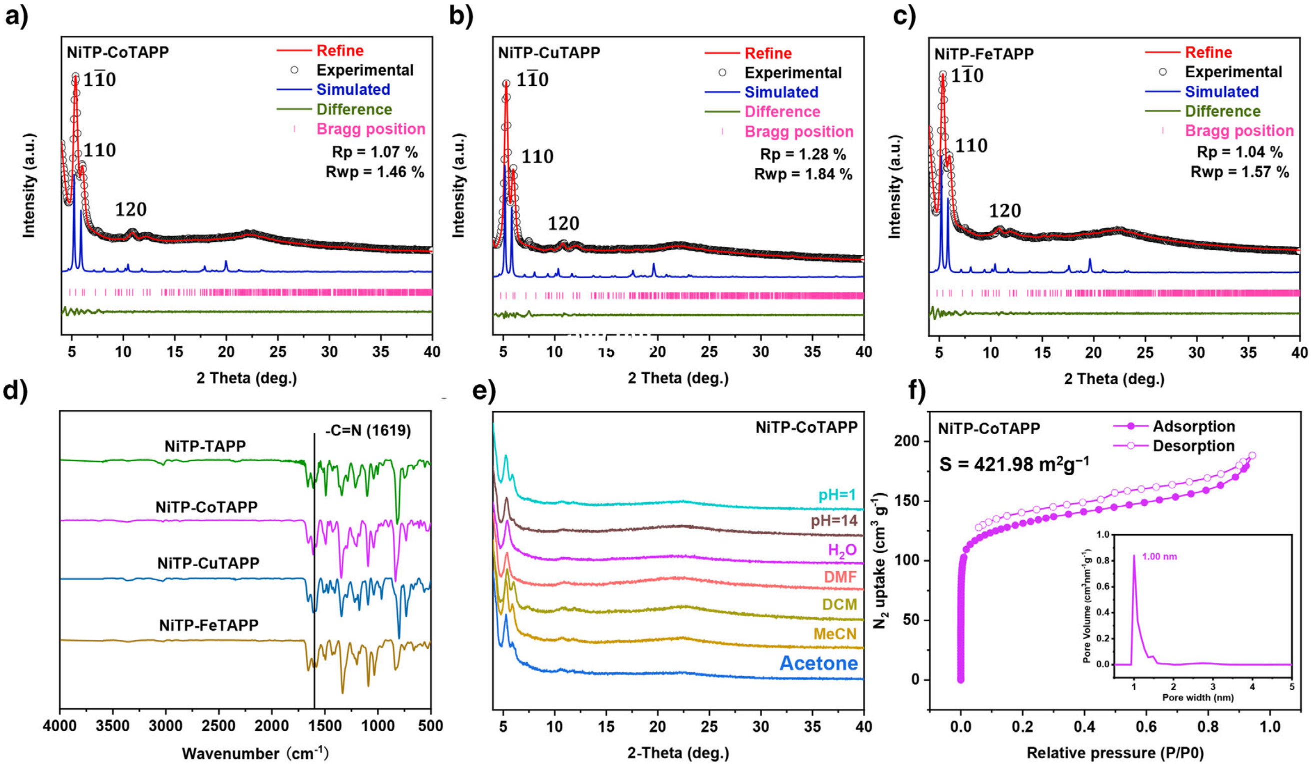

Figure 2. Structural characterization. a)–c) Experimental (black dot) and simulated (red line) PXRD patterns of NiTP-MTAPP (M = Co, Cu, and Fe). d) FTIR spectra of NiTP-MTAPP. e) PXRD patterns showing the stability of NiTP-CoTAPP. f) N_2 adsorption–desorption isotherms of NiTP-CoTAPP (inset pore-size distribution profile).

$R_{wp} = 1.84\%$ for NiTP-CuTAPP; Figure 2c, $R_p = 1.04\%$ and $R_{wp} = 1.57\%$ for NiTP-FeTAPP). The diffraction peaks at 5.13°, 8.04°, and 9.65° were assigned to the (1-10), (110), and (120) facets, respectively.

The successful synthesis of NiTP-TAPP and NiTP-MTAPP MCOFs (M = Co, Cu, and Fe) was confirmed by Fourier-transform infrared spectroscopy (FTIR). A new absorption peaks at 1619 cm^{-1}, which is a typical characteristic of the $-C{=}N$ bond.[31,33,58,59] The complete conversion of aldehyde ($-CHO$, $\sim 1695\ cm^{-1}$) and amine ($-NH_2$, $\sim 3200-3500\ cm^{-1}$) groups was verified by the disappearance of the $-N-H$ stretching vibrations and the $-C{=}O$ stretching vibrations from the reaction precursors (Figure 2d). Scanning electron microscopy (SEM) shows that they have uniform aggregation with small particle sizes and well-defined contours. The corresponding element mapping reveals the uniform distribution of Ni, Co, Cu, Fe, S, and N elements (Figure S3b). Additionally, taking NiTP-CoTAPP as an example, the structure of NiTP-CoTAPP was further confirmed by scanning transmission electron microscopy energy-dispersive X-ray spectroscopy (STEM-EDS, Figure S4) and high-resolution transmission electron microscopy (HRTEM, Figure S5). In the HRTEM image, rectangular lattice patterns were observed with an interlayer spacing (d-spacing) of 1.5 nm, which corresponds to the (1-10) crystallographic plane (approximately 16.7 Å deduced from PXRD).

Subsequently, to investigate the stability, PXRD experiments were conducted after soaking in different solvents and acid/alkali environments for 24 h. The results showed good tolerance of all MCOFs in water (H_2O), *N*,*N*-dimethylformamide (DMF), dichloromethane (DCM), acetonitrile (MeCN), acetone, 0.1 M HCI (acid solution with pH = 1), and 1 M KOH (alkaline solution with pH = 14) (Figures 2e and S6a–c). Confirmed by thermogravimetric analysis (TGA), their thermal stability temperatures are up to 300 °C (Figure S7). The ultraviolet–visible-near infrared absorption spectroscopy (UV–vis-NIR) analysis revealed a strong absorption of the [NiS_4] core in the near-infrared region, with a broad absorption peak. The porphyrin moiety exhibited a distinct absorption peak in the red-light region around 600 nm. The Tauc plot revealed that the incorporation of metals leads to a narrowing of the band gap in four MCOFs (the band gap of NiTP-TAPP is 1.15 eV). Among bimetallic MCOFs, NiTP-CoTAPP exhibits the narrowest band gap at 0.84 eV, followed by NiTP-CuTAPP at 0.93 eV and NiTP-FeTAPP at 1.07 eV (Figure S8a–d). Compared to the Tauc plot of NiPh-CoTAPP MCOF (1.03 eV, Figure S8e), the substitution of the phenyl group with a thiophene group results in a red shift in the absorption peak and a narrowing of the band gap, indicating more favorable electron transfer along the conduction pathway within the MCOF structure. Notably, the coordination of Co, Cu, and Fe ions with porphyrins extends the conjugation of the system, and the electronic interactions between the metal ions and porphyrins enhance the electron conductivity. Moreover, these metal ions can function as charge carriers in catalytic processes, thereby promoting electron transfer. The electrical conductivities at room temperature were determined to be 5.65×10^{-8}, 4.67×10^{-7}, 4.20×10^{-7}, and 1.25×10^{-7} S cm^{-1} for NiTP-TAPP, NiTP-CoTAPP, NiTP-CuTAPP, and NiTP-FeTAPP, respectively (Figure S9a–d). Compared to the conductivity of NiPh-CoTAPP MCOF (1.09×10^{-7} S cm^{-1}),[31] the introduction of thiophene groups in NiTP-CoTAPP increases the content of S-heteroatoms in the system, resulting in a fourfold increase in electrical conductivity (Figure S9e). N_2 adsorption measurements were performed at 77 K to evaluate the porosity and surface area of four MCOFs. All of them exhibited typical type I isotherms, revealing their microporous structures. The Brunauer–Emmett–Teller (BET) specific surface areas of NiTP-TAPP, NiTP-CoTAPP, NiTP-CuTAPP, and NiTP-FeTAPP were calculated to be 422.12, 421.98, 345.03, and 223.81 $m^2\ g^{-1}$, respectively (Figures 2f and S10). The BET surface area of NiTP-CuTAPP and NiTP-FeTAPP has decreased, which may be attributed to the high material density produced by Cu and Fe atoms and the decrease in crystallization. The slight desorption hysteresis and tilt can be attributed to the formation of macropores and mesopores resulting from the aggregation and stacking of covalent organic framework nanoparticles. The analysis of pore size distribution according to the N_2 density functional theory (DFT) model indicated that the pore size of each MCOF was estimated to be 1.00 nm.

Electrocatalytic NITRR Measurements

The electrocatalytic performance for NITRR was evaluated using three distinct NiTP-MTAPP MCOFs (M = Co, Cu, and Fe) electrodes in an H-type cell under ambient conditions. Figure 3a illustrates the linear sweep voltammetry (LSV) results for these electrodes tested in a pure nitrate (0.5 M KNO_3) solution, highlighting their varying efficiencies in nitrate reduction. In the H-cell with pure NO_3^- solution, the current output is dominated by the faradaic process of NITRR, which is significantly higher than the nonfaradaic background current expected from KCl (Figure S11, where no NITRR occurs). This confirms that the measured current in the NO_3^- system reflects the target electrocatalytic reaction rather than merely ohmic effects.

We conducted time-resolved current density measurements over a half-hour period under various applied overpotentials, as shown in Figures S12–S15. As anticipated, the current density steadily increased with more negative potentials. In evaluating ammonia production, the electrocatalytic activity of the three MCOF electrodes was ranked in the following order: NiTP-CoTAPP > NiTP-CuTAPP > NiTP-FeTAPP, as presented in Figure 3b. Notably, the NiTP-CoTAPP electrode demonstrated the highest faradaic efficiency of approximately 85.6% at −0.8 V (vs. RHE), paired with an impressive yield rate of 160.2 mmol $h^{-1}\ g^{-1}_{cat.}$ In comparison, NiTP-CuTAPP and NiTP-FeTAPP achieved optimal FEs of 76.3% and 70.8%, respectively. Furthermore, we investigated the electrochemical ammonia production activity of the NiS_4 unit. It was found that its performance in NO_2^- reduction surpasses that of NO_3^- reduction at various applied potentials (see Figure S16), indicating that NiS_4 exhibits a preferential tendency toward NO_2^- reduction. In the NiTP-CoTAPP system, NO_3^- reduction primarily occurs at the CoN_4 sites,

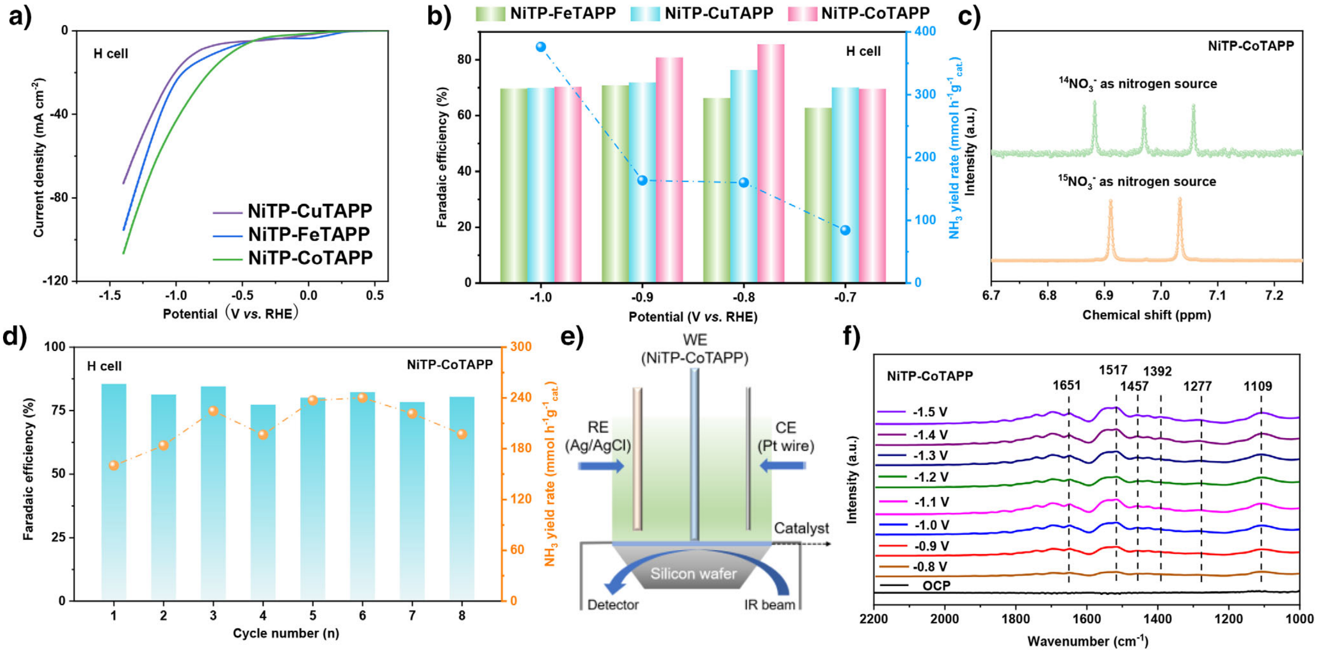

Figure 3. Electrocatalytic activities of NiTP-MTAPP (M = Co, Cu, and Fe) for the NITRR. a) LSV curves of NiTP-MTAPP electrodes (NiTP-CuTAPP, NiTP-FeTAPP, and NiTP-CoTAPP) tested in 0.5 M KNO_3 electrolyte and b) FE values (left *Y* axes) and corresponding NH_3 yield rates (right *Y* axes) of NiTP-MTAPP under various applied potentials for the NITRR. c) ^1H-NMR spectra of the products after the NITRR test of NiTP-CoTAPP electrocatalyst using $K^{14}NO_3$ and ^{15}N isotope-labeled $Na^{15}NO_3$ as the feeding nitrogen sources, respectively. d) The cycling tests of NiTP-CoTAPP electrocatalyst for NITRR tests at −0.8 V (vs. RHE) in a 0.5 M KNO_3 electrolyte. e) Schematic illustration of the apparatus for in situ electrochemical ATR-FTIR characterizations. f) In situ electrochemical ATR-FTIR spectra of NiTP-CoTAPP electrocatalyst under various potentials, respectively.

while the NiS_4 sites mimic the function of nitrite reductase (ferredoxin), further accelerating the conversion of NO_2^-. The CoN_4–NiS_4 system operates via a cascade catalysis mechanism, where the bimetallic interaction optimizes reaction kinetics, thereby enhancing both the ammonia production rate and selectivity. Additionally, we examined how varying nitrate concentrations in the electrolyte impacted ammonia production. In a mixed electrolyte of 0.1 M Na_2SO_4 and 0.1 M KNO_3, the ammonia production capacity of the NiTP-CoTAPP electrode significantly decreased across different applied overpotentials, as shown in Figures S17 and S18.

To confirm the source of ammonia production, we performed a ^{15}N isotope-labeling experiment using $^{15}NO_3^-$ reagent. The ^1H NMR spectra of the electrolyte containing $^{15}NO_3^-$ after the electrocatalytic NITRR are presented in Figure 3c, revealing distinct double peaks for $^{15}NH_4^+$. In contrast, when using $^{14}NO_3^-$ as the nitrogen source, we observed a triplet coupling peak for $^{14}NH_4^+$. This indicates that the ammonia generated during electrochemical reactions originated from the dissolved nitrate ions. Stability is a crucial factor in assessing the performance of an electrocatalyst. We evaluated the stability of the NiTP-CoTAPP catalyst through cycling tests, as shown in Figure 3d. After eight cycles, the FE for ammonia production at −0.8 V (vs. RHE) remained stable in the 0.5 M KNO_3 solution, exhibiting only minor variations throughout the cycles. When comparing the electrocatalytic performance of the NiTP-CoTAPP catalyst with prior electrode materials, our findings demonstrate that it surpasses many representative catalysts for ammonia electrosynthesis in terms of FE values, as displayed in Figure S19.

To enhance our understanding of the fundamental mechanisms underlying electrocatalysis in the NITRR, we utilized in situ attenuated total reflectance Fourier transform infrared (ATR-FTIR) spectroscopy, as illustrated in Figure 3e. The ATR-FTIR data for the NiTP-CoTAPP electrocatalyst, collected using a three-electrode setup across applied potentials of −0.8 to −1.5 V (vs. RHE), is shown in Figure 3f. The spectrum reveals a peak near 1457 cm^{-1}, corresponding to the σ(N−H) bending mode of ammonium (NH_4^+), which indicates the hydrogenation processes that facilitate ammonia production after the reduction of nitrate.[60–64] Another significant band at 1392 cm^{-1} correlates with the stretching mode of nitrate (NO_3^-), illustrating its consumption throughout the reaction. Additionally, we detected several positive peaks that signify various nitrogen-containing intermediates. Specifically, the peak at 1277 cm^{-1} relates to the N─O antisymmetric stretching vibration of nitrite (NO_2^-), suggesting its formation during the reduction of nitrate.[65–69] Another intermediate is indicated by a peak around 1109 cm^{-1}, which can be attributed to the ─N─O─ stretching vibration of *ONH_2, an important precursor in ammonia synthesis.[62,69,70] Moreover, peaks at 1517 and 1651 cm^{-1} are associated with the stretching mode of nitric oxide (NO), highlighting critical deoxygenation steps involved in nitrate reduction.[60,61,65,66,71]

The effective application of the engineered electrocatalyst for NITRR relies on achieving current densities that meet industrial standards. To facilitate the transition from laboratory-scale prototypes to large-scale implementation of NITRR technology, the development of a flow cell system is essential. In this study, we designed a custom flow cell

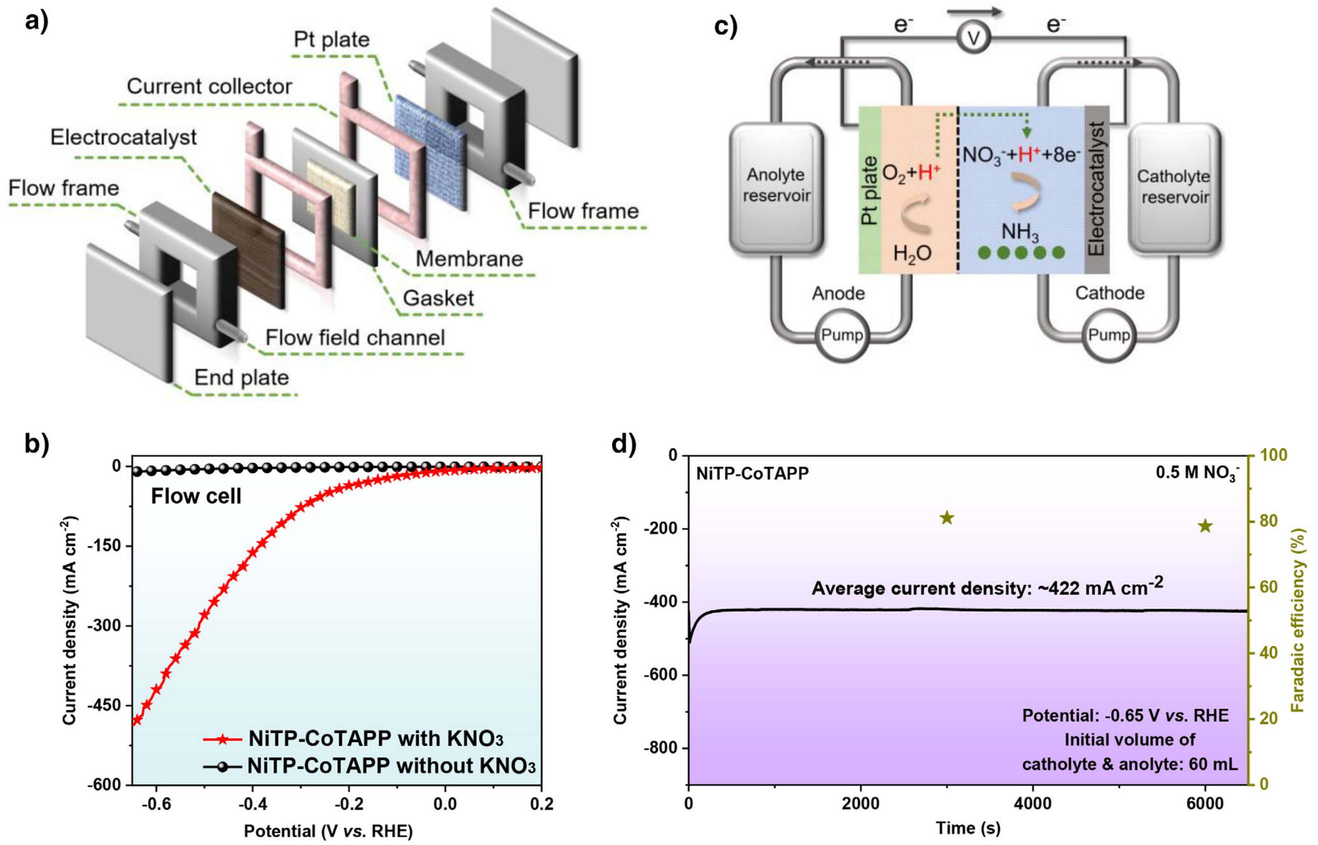

Figure 4. The NITRR test in flow cell. a) and b) Schematic illustration of the flow cell system. c) LSV curves of NiTP-CoTAPP electrocatalyst tested in the flow cell using aqueous electrolytes of 0.5 M KCl and 0.5 M KNO_3, respectively. d) Time-dependent industrially relevant current density curve of NiTP-CoTAPP electrocatalyst at an applied potential of −0.65 V (vs. RHE).

specifically for testing the electrocatalytic NITRR, as depicted in Figure 4a,b. Linear sweep voltammetry (LSV) analysis of the NiTP-CoTAPP electrocatalyst, conducted in a 0.5 M KNO_3 solution, demonstrated a significantly higher current density compared to that in a 0.5 M KCl solution across the potential range of 0.2 to −0.65 V (vs. RHE), confirming the successful implementation of NITRR (see Figure 4c). Further, we assessed the time-dependent current density of the NiTP-CoTAPP electrocatalyst over a 6500-s operational period at −0.65 V (vs. RHE). As shown in Figure 4d, the average current density reached approximately 422 mA cm^{-2}, with no significant decline in the faradaic efficiency for ammonia production during this interval. Specifically, the designed NiTP-CoTAPP electrocatalyst achieves a faradaic efficiency of 81.1% toward selective ammonia production within a reaction time of 3000 s; the value remains at 78.6% after 6000 s, accompanied by a high ammonia production rate of 3101.7 mmol h^{-1} $g^{-1}{}_{cat}$.

DFT Calculations of NITRR Pathways

The reduction of NO_3^- to NH_3 is a complex multielectron process that involves multiple potential intermediate species. Among them, $^*NO_3$, $^*NO_2$, and NO are widely regarded as the most important intermediates in this process.[72] Experimentally, it has been observed that the activity order of different catalysts is NiTP-CoTAPP > NiTP-CuTAPP > NiTP-FeTAPP. As shown in Figures 5a, S20, and S21, the density functional theory (DFT) calculation method was utilized to deeply explore the relationship between the electronic structures and catalytic performances of the Cu, Co, and Fe active centers. The NITRR process of NiTP-MTAPP includes sequential deoxygenation steps to form *N and subsequent hydrogenation steps to produce NH_3, and NiTP-MTAPP exhibits a relatively smooth reaction path throughout. However, for both Fe and Co active centers, the rate-determining steps (RDS) is the transformation of NO_3^- to $^*NO_3$, whereas for Cu active center, the hydrogenation of $^*HNO_2$ is considered as the RDS. The energy barrier for the RDS of NO_3^- to $^*NO_3$ on the Co active center is 0.56 eV, which is the lowest. The energy barrier for the Cu active center in the step of $^*HNO_2$ to *NO is 0.66 eV, and that for the Fe active center in the step of NO_3^- to $^*NO_3$ is 0.72 eV, which is relatively high. The relatively small change in ΔG of the Co active site promotes the forward reaction, which is consistent with the experimental activity order. According to the volcano plot curve,[73] Co is most likely to have advantageous activity as it is very close to the peak of the volcano plot, which may be related to the moderate adsorption ability of the CoN_4 site. The closer the d-band center is to the Fermi level, the stronger the adsorption

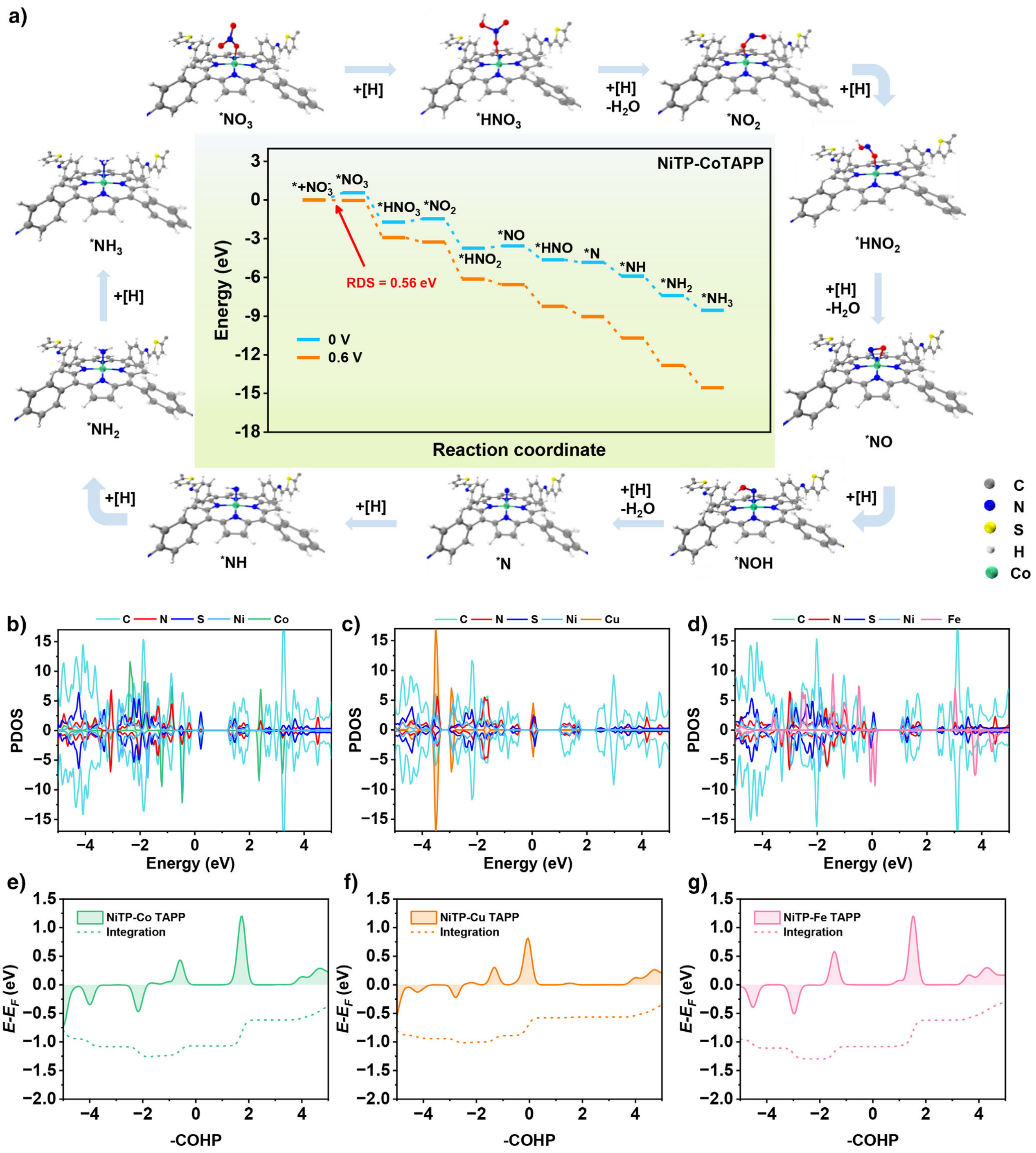

Figure 5. a) Free energy diagram of electrochemical NO_3^- conversion in NiTP-CoTAPP; b)–d) projected density of states (PDOS) of NiTP-CoTAPP, NiTP-CuTAPP, and NiTP-FeTAPP; e)–g) projected crystal orbital Hamilton population (PCOHP) and integrated COHP (ICOHP) diagrams of NiTP-CoTAPP, NiTP-CuTAPP, and NiTP-FeTAPP.

ability of the metal for the reactant. However, overly strong adsorption may lead to difficulty in desorption of the reactant, which is not conducive to the catalytic cycle. Therefore, the d-band centers of the three metal sites within this system were computed via the DOS results. As shown in Figure S22, the d-band center of Cu was determined to be −3.26 eV and that of Fe was −1.21 eV. In comparison to Co (−1.68 eV), Cu resides relatively farther from the Fermi level, whereas Fe is relatively closer. This correspondingly indicates a relatively feeble adsorption capacity for the intermediate in the case of Cu and a relatively robust one for Fe. As shown in Figure 5b–d, the PDOS results more intuitively reflect the moderate electron density of Co near the Fermi energy level, which is the key to the rapid and continuous process of nitrate and its intermediate desorption–adsorption dynamics. Co exhibits a moderately positioned d-band center, a characteristic notably consistent with the adsorption-energy requirements outlined in the Sabatier principle. This electronic configuration creates an optimal adsorption–desorption equilibrium that facilitates catalytic activity. Particularly in this reaction system, the distinctive electronic structure of Co appears to critically govern the catalytic efficiency by maintaining this crucial energetic balance between reactant activation and product release. The order of the Bader charge values is Fe > Co > Cu (Cu is -0.96 e, Co is -1.03 e, and Fe is -1.10 e), further indicating the regulatory effect of the Co catalytic center site on the adsorption ability of the intermediate (Figure S23a–c).

Electron density difference (EDD) results (Figure S24) indicate that Fe, Co, and Cu all exhibit robust electronic interactions with the adjacent N within the coordination environment, implying that all three catalytic sites possess relatively high stability. The DFT results suggest that the catalytic active centers of NiTP-MTAPP all possess potential catalytic performance, and the distinctive catalytic active center of NiTP-CoTAPP achieves even more exceptional catalytic performance via the modulation of the adsorption capacity of the adsorbed species. The computed results of the Crystal Orbital Hamilton Population (COHP) analysis reveal that the three metal sites exhibit comparable bonding states when coordinating with nitrogen (N),[74] as depicted in Figure 5e–g. Notably, the interaction between Co and N is stronger. With respect to the hydrogen evolution reaction (HER), the computational findings indicate that the Co and Fe sites display relatively low Gibbs free energy of hydrogen adsorption (ΔG) values of 0.12 and 0.48 eV, respectively. Consequently, under neutral conditions, a higher quantity of protonated hydrogen is generated, which in turn facilitates a synergistic reaction with the NITRR and subsequently reduces the reaction energy barrier. In contrast, the Cu site demonstrates inferior HER performance ($\Delta G = 1.98$ eV). While this diminishes the competitiveness between the HER and NITRR, it also fails to provide an adequate supply of *H to sustain the surface hydrogenation rate of the catalyst, thereby adversely affecting the reduction of oxynitride intermediates (Figure S25). Consequently, the catalytic activity of NiTP-CuTAPP is lower in comparison to that of NiTP-CoTAPP but remains higher than that of NiTP-FeTAPP.

Conclusion

In summary, we have synthesized a series of 2D NiTP-MTAPP MCOFs (M = 2H, Co, Cu, and Fe), with well-defined structures and atomically dispersed dual catalytic active sites, based on the redox-active ligand-Ni[$C_2S_2(C_4H_2SCHO)_2$]$_2$, through the regulation of presynthesized metalloporphyrin linkers. The introduction of thiophene groups and metal ions facilitated charge transfer and increased the carrier concentration. After design and screening, NiTP-CoTAPP exhibited the optimal NITRR performance, with a NH_3 production rate of 160.2 mmol h^{-1} $g^{-1}_{cat.}$ and a faradaic efficiency of 85.6%. The CoN_4 sites efficiently absorbed and reduced NO_3^-, while the NiS_4 sites mimicked nitrite reductase, further promoting the conversion of NO_2^- intermediates. The bimetallic framework structure offered exceptional catalytic water stability and high atom economy. Additionally, the supply of active hydrogen at NiS_4 sites achieved dynamic equilibrium with the timely hydrogenation reaction at CoN_4 sites, effectively suppressing the HER and enhancing ammonia selectivity. DFT calculations revealed three distinct catalytic pathways, with the CoN_4 sites exhibiting the optimal adsorption-to-desorption and the lowest catalytic energy barrier, which was supported by the moderate d-band center and Bader charge values. This study provides novel insights into the modular design of highly efficient bimetallic MCOFs-based catalysts for nitrate reduction.

Acknowledgements

This work was supported by the National Natural Science Foundation of China (22275084, 22479074, 22425106, and 22475096), the Natural Science Foundation of Jiangsu Province (BK20243010, BK20240400, and BK20241236), the General Project of the Joint Fund of Equipment Preresearch and the Ministry of Education (8091B02052407), the Science and Technology Major Project of Jiangsu Province (BG2024013), the Scientific and Technological Achievements Transformation Special Fund of Jiangsu Province (BA2023037), the Academic Degree and Postgraduate Education Reform Project of Jiangsu Province (JGKT24_C001), the Key Core Technology Open Competition Project of Suzhou City (SYG2024122), the Open Research Fund of Suzhou Laboratory (SZLAB-1308-2024-TS005), the Gusu Leading Talent Program of Scientific and Technological Innovation and Entrepreneurship of Wujiang District in Suzhou City (ZXL2021273), and the Chenzhou National Sustainable Development Agenda Innovation Demonstration Zone Provincial Special Project (2023sfq11).

Conflict of Interests

The authors declare no conflict of interest.

Data Availability Statement

The data that support the findings of this study are available in the Supporting Information of this article.

Keywords: Adsorption-to-desorption • Dithiolene complexes • Electrocatalytic nitrate reduction • Metalized covalent organic framework • Redox-active

---

[1] Y. Ashida, K. Arashiba, K. Nakajima, Y. Nishibayashi, *Nature* **2019**, *568*, 536–540.

[2] K. Fan, W. Xie, J. Li, Y. Sun, P. Xu, Y. Tang, Z. Li, M. Shao, *Nat. Commun.* **2022**, *13*, 7958.
[3] M. Wang, S.-F. Li, Y.-M. Gu, W.-J. Xu, H.-Z. Wang, J.-J. Sun, S.-M. Chen, Z.-X. Tie, J.-L. Zuo, J. Ma, J. Su, Z. Jin, *J. Am. Chem. Soc.* **2024**, *146*, 20439–20448.
[4] P. H. Van Langevelde, I. Katsounaros, M. T. M. Koper, *Joule* **2021**, *5*, 290–294.
[5] Y. Liu, M. Cheng, Z. He, B. Gu, C. Xiao, T. Zhou, Z. Guo, J. Liu, H. He, B. Ye, B. Pan, Y. Xie, *Angew. Chem. Int. Ed.* **2019**, *58*, 731–735.
[6] Z. Y. Wu, M. Karamad, X. Yong, Q. Huang, D. A. Cullen, P. Zhu, C. Xia, Q. Xiao, M. Shakouri, F. Y. Chen, J. Y. T. Kim, Y. Xia, K. Heck, Y. Hu, M. S. Wong, Q. Li, I. Gates, S. Siahrostami, H. Wang, *Nat. Commun.* **2021**, *12*, 2870.
[7] C. Lv, C. Yan, G. Chen, Y. Ding, J. Sun, Y. Zhou, G. Yu, *Angew. Chem. Int. Ed.* **2018**, *57*, 6073–6076.
[8] M. Kitano, Y. Inoue, Y. Yamazaki, F. Hayashi, S. Kanbara, S. Matsuishi, T. Yokoyama, S.-W. Kim, M. Hara, H. Hosono, *Nat. Chem.* **2012**, *4*, 934–940.
[9] M. Jiang, L. Han, P. Peng, Y. Hu, Y. Xiong, C. Mi, Z. Tie, Z. Xiang, Z. Jin, *Nano Lett.* **2022**, *22*, 372–379.
[10] J. Zheng, F. Liao, S. Wu, G. Jones, T. Y. Chen, J. Fellowes, T. Sudmeier, I. J. McPherson, I. Wilkinson, S. C. E. Tsang, *Angew. Chem. Int. Ed.* **2019**, *58*, 17335–17341.
[11] G.-F. Chen, Y. Yuan, H. Jiang, S.-Y. Ren, L.-X. Ding, L. Ma, T. Wu, J. Lu, H. Wang, *Nat. Energy* **2020**, *5*, 605–613.
[12] M. D. Victor Rosca, M. T. de Groot, Marc T. M. Koper, *Chem. Rev.* **2009**, *109*, 2209–2244.
[13] E. D. Glendening, A. M. Halpern, *J. Chem. Phys.* **2007**, *127*, 164307.
[14] R. Hawtof, S. Ghosh, E. Guarr, C. Xu, R. Mohan Sankaran, J. N. Renner, *Sci. Adv.* **2019**, *5*, eaat5778.
[15] Y. Ren, C. Yu, L. Wang, X. Tan, Z. Wang, Q. Wei, Y. Zhang, J. Qiu, *J. Am. Chem. Soc.* **2022**, *144*, 10193–10200.
[16] J. Li, G. Zhan, J. Yang, F. Quan, C. Mao, Y. Liu, B. Wang, F. Lei, L. Li, A. W. M. Chan, L. Xu, Y. Shi, Y. Du, W. Hao, P. K. Wong, J. Wang, S. X. Dou, L. Zhang, J. C. Yu, *J. Am. Chem. Soc.* **2020**, *142*, 7036–7046.
[17] Y. Lv, J. Su, Y.-M. Gu, B.-L. Tian, J. Ma, J.-L. Zuo, M.-N. Ding, *JACS Au* **2022**, *2*, 2765–2777.
[18] N. Gruber, J. N. Galloway, *Nature* **2008**, *451*, 293–296.
[19] C. Liu, H. Li, F. Liu, J.-S. Chen, Z.-X. Yu, Z.-W. Yuan, C.-J. Wang, H.-L. Zheng, G. Henkelman, L. Wei, Y. Chen, *J. Am. Chem. Soc.* **2020**, *142*, 21861–21871.
[20] W.-S Gao, K.-F. Xie, J. Xie, X.-M. Wang, H. Zhang, S.-Q. Chen, H. Wang, Z.-L. Li, C. Li, *Adv. Mater.* **2023**, *35*, 2202952.
[21] L.-B. Qin, F. Sun, Z.-H. Gong, G.-Y. Ma, Y. Chen, Q. Tang, L. Qiao, R.-H. Wang, Z.-Q. Liu, Z.-H. Tang, *ACS Nano* **2023**, *17*, 12747–12758.
[22] J. Zhang, W.-H. He, T. Quast, J. R. C. Junqueira, S. Saddeler, S. Schulz, W. Schuhmann, *Angew. Chem. Int. Ed.* **2023**, *135*, e202214830.
[23] L.-H. Xu, W.-P. Liu, K. Liu, *Adv. Funct. Mater.* **2023**, *33*, 2304468.
[24] X. Wang, X. Han, C. Cheng, X. Kang, Y. Liu, Y. Cui, *J. Am. Chem. Soc.* **2022**, *144*, 7366–7373.
[25] S. Haldar, M. Wang, P. Bhauriyal, A. Hazra, A. H. Khan, V. Bon, M. A. Isaacs, A. De, L. Shupletsov, T. Boenke, J. Grothe, T. Heine, E. Brunner, X. Feng, R. Dong, *J. Am. Chem. Soc.* **2022**, *144*, 9101–9112.
[26] X. Guan, H. Li, Y. Ma, M. Xue, Q. Fang, Y. Yan, V. Valtchev, S. Qiu, *Nat. Chem.* **2019**, *11*, 587–594.
[27] H. Lyu, C. S. Diercks, C.-H. Zhu, O. M. Yaghi, *J. Am. Chem. Soc.* **2019**, *141*, 6848–6852.
[28] G. Lin, H. Ding, R. Chen, Z. Peng, B. Wang, C. Wang, *J. Am. Chem. Soc.* **2017**, *139*, 8705–8709.
[29] T. Tanaka, A. Osuka, *Chem. Soc. Rev.* **2015**, *44*, 943–969.
[30] Y.-J. Wang, D.-M. Song, J. Li, Q. Shi, J.-L. Zhao, Y.-P. Hu, F.-L. Zeng, N. Wang, *Inorg. Chem.* **2022**, *61*, 10198–10204.
[31] S.-W. Ke, W. Li, Y.-M. Gu, J. Su, Y.-F. Liu, S. Yuan, J.-L. Zuo, J. Ma, P. He, *Sci. Adv.* **2023**, *9*, eadf2398.
[32] S. Suleman, X.-Y. Guan, Y. Zhang, A. Waseem, O. Metin, Z. Meng, H.-L. Jiang, *Chem. Eng. J.* **2023**, *476*, 146623.
[33] M. Lu, J. Liu, Q. Li, M. Zhang, M. Liu, J.-L. Wang, D.-Q. Yuan, Y.-Q. Lan, *Angew. Chem. Int. Ed.* **2019**, *58*, 12392–12397.
[34] N. B. Aetukuri, B. D. McCloskey, J. M. García, L. E. Krupp, V. Viswanathan, A. C. Luntz, *Nat. Chem.* **2015**, *7*, 50–56.
[35] C. Zheng, W. Ding, C. Wang, *J. Mater. Chem. A* **2019**, *7*, 6180–6186.
[36] D.-J. Fa, J.-Y. Yuan, G.-Y. Feng, S.-B. Lei, W.-P. Hu, *Angew. Chem. Int. Ed.* **2023**, *62*, e202300532.
[37] D. P. Butcher, A. A. Gewirth, *Nano Energy* **2016**, *29*, 457–465.
[38] J.-X. Liu, D. Richards, N. Singh, B. R. Goldsmith, *ACS Catal.* **2019**, *9*, 7052–7064.
[39] Y. Wang, C. Wang, M. Li, Y. Yu, B. Zhang, *Chem. Soc. Rev.* **2021**, *50*, 6720–6733.
[40] M. Duca, M. T. M. Koper, *Energy Environ. Sci.* **2012**, *5*, 9726.
[41] Y. Jiang, J. Yang, M.-L. Li, X.-J. Wang, N. Yang, W.-P. Chen, J.-C. Dong, J.-F. Li, *Chin. J. Catal.* **2024**, *59*, 195–203.
[42] W. Zheng, D.-G. Fan, Y. Yang, Q.-W. Chen, *Nano Lett.* **2024**, *24*, 9011–9016.
[43] H.-B. Yin, F. Dong, H.-W. Su, Z.-C. Zhuang, Y.-L. Wang, D.-S. Wang, Y. Peng, J.-H. Li, *ACS Nano* **2023**, *17*, 25614–25624.
[44] M. Liu, Z.-H. Lu, L.-H. Yang, R.-M. Gao, X.-Y. Zhang, Y.-J. Wang, Y.-H. Wang, *J. Environ. Chem. Eng.* **2023**, *11*, 109718.
[45] L.-L. Lv, Y.-Q. Shen, M. Zhou, Y. Zhang, X.-H. Meng, X. Yang, N. Zhang, K.-X. Wang, Q.-R. He, D.-W. Gong, Q. Ai, Y. Shuai, Z.-X. Zhou, *J. Mater. Chem. A* **2024**, *12*, 6733–6746.
[46] F. Rehman, S. Kwon, C. B. Musgrave, M. Tamtaji, W. A. Goddard, Z.-T. Luo, *Nano Energy* **2022**, *103*, 107866.
[47] S.-B. Zhang, Y.-F. Wu, Y.-X. Zhang, Z.-Q. Niu, *Mater. Sci. Eng. R Rep.* **2025**, *16*, 100886.
[48] J.-Q. Dong, X. Han, Y. Liu, H.-Y. Li, Y. Cui, *Angew. Chem. Int. Ed.* **2020**, *59*, 13722–13733.
[49] L.-S. Sun, M. Lu, Z.-F. Yang, Z.-Y. Yu, X. Su, Y.-Q. Lan, L. Chen, *Angew. Chem. Int. Ed.* **2022**, *61*, e202204326.
[50] H.-Y. Hu, R.-Y. Miao, F.-L. Yang, F. Duan, H. Zhu, Y.-M. Hu, M.-L. Du, S.-L. Lu, *Adv. Energy Mater.* **2024**, *14*, 2302608.
[51] F. Lv, M.-Z. Sun, Y.-P. Hu, J. Xu, W. Huang, N. Han, Y.-G. Li, B.-L. Huang, *Energy Environ. Sci.* **2023**, *16*, 201–209.
[52] Y. Wang, A. Xu, Z. Wang, L. Huang, J. Li, F. Li, J. Wicks, M. Luo, D. H. Nam, C. S. Tan, Y. Ding, J. Wu, Y. Lum, C. T. Dinh, D. Sinton, G. Zheng, E. H. Sargent, *J. Am. Chem. Soc.* **2020**, *142*, 5702–5708.
[53] K. Liu, H.-M. Li, M.-H. Xie, P.-F. Wang, Z.-Y. Jin, Y.-T. Liu, M. Zhou, P.-P. Li, G.-H. Yu, *J. Am. Chem. Soc.* **2024**, *146*, 7779–7790.
[54] Z.-D. Zhang, Y. Lv, Y.-M. Gu, X.-C. Zhou, B.-L. Tian, A.-Q. Zhang, Z.-M. Yang, S.-Z. Chen, J. Ma, M.-N. Ding, J.-L. Zuo, *Angew. Chem. Int. Ed.* **2024**, *64*, e202418272.
[55] Z.-M. Yang, Y.-D. Wang, M.-H. Zhang, Z.-Y. Hou, S.-P. Zhao, X. Han, S. Yuan, J. Su, Z. Jin, J.-L. Zuo, *Energy Storage Mater.* **2025**, *75*, 104038.
[56] J. Rivnay, S. Inal, B. A. Collins, M. Sessolo, E. Stavrinidou, X. Strakosas, C. Tassone, D. M. Delongchamp, G. G. Malliaras, *Nat. Commun.* **2016**, *7*, 11287.
[57] H. Meng, D. F. Perepichka, F. Wudl, *Angew. Chem. Int. Ed.* **2003**, *42*, 658–661.
[58] S. Lv, X.-K. Ma, S.-W. Ke, Y.-D. Wang, T.-R. Ma, S. Yuan, Z. Jin, J.-L. Zuo, *J. Am. Chem. Soc.* **2024**, *146*, 9385–9394.
[59] Y.-Y. Li, T.-Q. Wei, C. Liu, Z.-D. Zhang, L.-F. Wu, M.-N. Ding, S. Yuan, J. Zhu, J.-L. Zuo, *Chem. Eur. J.* **2023**, *29*, e202301048.

[60] Z.-M. Song, Y. Liu, Y.-Z. Zhong, Q. Guo, J. Zeng, Z.-G. Geng, *Adv. Mater.* **2022**, *34*, 2204306.
[61] N. Zhang, J. Shang, X. Deng, L.-J. Cai, R. Long, Y.-J. Xiong, Y. Chai, *ACS Nano* **2022**, *16*, 4795–4804.
[62] E. Pérez-Gallent, M. C. Figueiredo, I. Katsounaros, M. T. M. Koper, *Electrochim. Acta* **2017**, *227*, 77–84.
[63] N. Zhang, A. Jalil, D.-X. Wu, S.-M. Chen, Y.-F. Liu, C. Gao, W. Ye, Z.-M. Qi, H.-X. Ju, C.-M. Wang, X.-J. Wu, L. Song, J.-F. Zhu, Y.-J. Xiong, *J. Am. Chem. Soc.* **2018**, *140*, 9434–9443.
[64] Y.-Z. Zhang, H. Zheng, K.-J. Zhou, J.-Y. Ye, K.-B. Chu, Z.-Y. Zhou, L.-S. Zhang, T.-X. Liu, *Adv. Mater.* **2023**, *35*, 2209855.
[65] S.-E. Bae, K. L. Stewart, A. A. Gewirth, *J. Am. Chem. Soc.* **2007**, *129*, 10171–10180.
[66] M. C. Figueiredo, J. Solla-Gullón, F. J. Vidal-Iglesias, V. Climent, J. M. Feliu, *Catal. Today* **2013**, *202*, 2–11.
[67] R. Hao, L. Tian, C. Wang, L. Wang, Y.-P. Liu, G.-C. Wang, W. Li, G. A. Ozin, *Chem. Catal.* **2022**, *2*, 622–638.
[68] M. C. Figueiredo, J. Souza-Garcia, V. Climent, J. M. Feliu, *Electrochem. Commun.* **2009**, *11*, 1760–1763.
[69] J.-Y. Fang, Q.-Z. Zheng, Y.-Y. Lou, K.-M. Zhao, S.-N. Hu, G. Li, O. Akdim, X.-Y. Huang, S.-G. Sun, *Nat. Commun.* **2022**, *13*, 7899.
[70] V. Rosca, G. L. Beltramo, M. T. M. Koper, *J. Electroanal. Chem.* **2004**, *566*, 53–62.
[71] L. Chen, J.-H. Li, M.-F. Ge, *Environ. Sci. Technol.* **2010**, *44*, 9590–9596.
[72] W.-D. Chen, X.-Y. Yang, Z.-D. Chen, Z.-J. Ou, J.-T. Hu, Y. Xu, Y.-L. Li, X.-Z. Ren, S.-H. Ye, J.-S. Qiu, J.-H. Liu, Q.-L. Zhang, *Adv. Funct. Mater.* **2023**, *33*, 2300512.
[73] N. C. Kani, J. A. Gauthier, A. Prajapati, J. Edgington, I. Bordawekar, W. Shields, M. Shields, L. C. Seitz, A. R. Singh, M. R. Singh, *Energy Environ. Sci.* **2021**, *14*, 6349–6359.
[74] R. Dronskowski, P. E. Bloechl, *J. Phys. Chem.* **1993**, *97*, 8617–8624.

Manuscript received: March 10, 2025
Revised manuscript received: April 07, 2025
Accepted manuscript online: April 22, 2025
Version of record online: May 05, 2025